

NASA
Technical
Paper
2946

AVSCOM
Technical
Memorandum
89-B-010

January 1990

AD-A219 296

Rotor Induced-Inflow-Ratio
Measurements and
CAMRAD Calculations

DTIC
ELECTE
MAR 15 1990
S D
D cy

Danny R. Hoad

*Original contains color
plates: All DTIC reproductions
will be in black and
white*



DISTRIBUTION STATEMENT A

Approved for public release
Distribution Unlimited

NASA

90 03rd 14 015

**NASA
Technical
Paper
2946**

**AVSCOM
Technical
Memorandum
89-B-010**

1990

**Rotor Induced-Inflow-Ratio
Measurements and
CAMRAD Calculations**

Danny R. Hoad
*Aerostructures Directorate
USAARTA-AVSCOM
Langley Research Center
Hampton, Virginia*

Accession For	
NTIS	CRA&I <input checked="" type="checkbox"/>
DTIC	TAB <input type="checkbox"/>
Unannounced	<input type="checkbox"/>
Justification	
By	
Distribution /	
Availability Codes	
Dist	Avail and/or Special
A-1	



National Aeronautics and
Space Administration
Office of Management
Scientific and Technical
Information Division



Summary

The results of a comparison between CAMRAD (Comprehensive Analytical Model of Rotorcraft Aerodynamics and Dynamics) and rotor inflow measurements using a laser velocimeter have been presented. This information is presented for a rectangular four-bladed rotor system operating at a thrust coefficient of 0.0064. The inflow measurements were made at azimuthal increments of 30° from an azimuth (Ψ) of 0° at 3.0 in. (approximately one chord) above the plane formed by the tips of the blades. Measurements were made from radial locations of the local radius nondimensionalized by a rotor radius of 0.2 to 1.1; the majority of the measurement locations were concentrated toward the outboard portion of the disc. The measurements included time-averaged induced-inflow characteristics and conditionally sampled data. The model used in the CAMRAD code utilized the "Scully Free-Wake" option. Two rotor-trim options were used in the analysis.

The experimental measurements showed that as the advance ratio increased, the induced-upflow region moved progressively from the forward 20 percent of the rotor disc at an advance ratio (μ) of 0.15 to a point where it covered most of the forward half of the rotor disc at $\mu = 0.30$. The presence of the concentrated tip vortices and rollup of the wake structure was evident in the $\mu = 0.15$ data on both sides of the rotor disc; however, as the advance ratio was increased, the rollup process appeared to move farther outboard and the influence on the local induced velocities was reduced. The induced-inflow characteristics at all advance ratios were unsymmetrical about the longitudinal centerline. The maximum downwash was in the rear portion of the disc and was skewed to the advancing-blade side.

The comparisons with the analytical method at $\mu = 0.15$ show that the region of induced upflow over the front 20 percent of the rotor was effectively modeled. The evidence of the wake rollup process on both sides of the rotor system was also indicated. Comparisons at $\mu = 0.23$ and $\mu = 0.30$ showed the inability of the method to model the extent of the induced upflow measured over the forward portion of the rotor disc. CAMRAD consistently indicated that the largest values of induced-inflow ratio were on the retreating-blade side of the rotor disc—opposite from that measured. Computing the trim conditions based on rotor propulsive force did not improve the prediction of the extent of upflow at the higher advance ratios and did not change the prediction for location of maximum downwash.

An effective mean flow-angle difference was calculated from the difference in velocities computed analytically and measured. The difference in rotor-blade angle of attack is estimated to be no more than 1° for most of the operating conditions. There were, however, regions where the calculated differences were significant. The worst was in the region where the flow-angle difference was greater than 1° . At an advance ratio of 0.15, this region was relatively small, but as the advance ratio increased to 0.23 and 0.30, this region grew to an area that encompassed a large percentage of the third quadrant of the rotor disc. In these calculations, the method used for trim had very little effect on the overall results of the comparisons between measurement and analysis.

At each of the 180 measurement locations at each advance-ratio condition tested, data collected were conditionally sampled with rotor-blade position. Only a selected sample of these are presented. The time-history comparisons show the azimuthal resolution limitations in this version of CAMRAD. It was obvious that the limitations in the CAMRAD prediction resolution resulted in a considerable degradation of the inflow waveform compared with the measured data. The peak-to-peak variations of induced inflow near the blade cuff were not modeled well with the CAMRAD predictions; however, near the tip, the waveform appears to have been modeled well by both CAMRAD trim option calculations if the limitations in azimuthal resolution in the CAMRAD calculations are considered. It is important to recognize that the resolution limitations of CAMRAD do not capture the high gradients measured, particularly near the rotor-blade tip.

A global indication of the time-dependent inflow characteristics was provided by presenting the fourth harmonic of the order-ratio analyses of the measured and predicted induced-inflow ratio. The experimental data showed that the oscillatory inflow characteristics were at a maximum on the retreating-blade side of the rotor disc, particularly in the third quadrant between 180° and 270° azimuth. For all rotor test conditions, the oscillatory inflow on the advancing-blade side of the rotor disc was minimal.

The analytical predictions of oscillatory induced-inflow ratio indicated a remarkable similarity to the experimental data. At all advance ratios, the maximum oscillatory inflow was in the third quadrant, but at slightly higher values. The size of the maximum oscillatory inflow region for the analytical results was much larger than for those measured, particularly at an advance ratio of 0.23. The effects of the high-gradient inflow characteristics in the measured data were not shown here, since the contours were

presented only for the fourth harmonic (or blade-passage frequency) and the analyses were limited in resolution in the time domain.

Introduction

The inflow environment of a helicopter rotor system is affected by the circulation of the lifting blades, the trailing circulation in the wake, and the presence of the fuselage. This inflow environment affects the performance of the rotor system, which in turn changes the wake structure and the flow field in which the rotor, fuselage, and other surfaces must operate. Current computational tools for helicopter aerodynamic analysis that attempt to describe this environment and account for this interaction process, though sophisticated, are not well proven. Even the task of computing the rotor controls for trim and steady level flight with any degree of confidence on a day-to-day basis cannot be demonstrated. (See ref. 1.) An integral part of the more complex aerodynamic analyses for the prediction of rotorcraft performance is the calculation of induced velocities at the rotor plane that are used in the process of computing rotor-blade-segment angle of attack. (See ref. 2.) Because of this mutual interference process, a priori knowledge of the induced inflow to the rotor system in the performance prediction process is equivalent to a priori knowledge of the results of the performance analysis.

The design tools in use today, similar to those of reference 2, typically utilize an iterative process between the performance calculations and rotor-wake induced-inflow velocity calculations. Some of these induced-inflow calculations utilize simplified assumptions that range from uniform inflow calculations based on momentum considerations to more complex approximations of the longitudinal and lateral variations of induced velocity over the rotor disc. (See ref. 3.) However, some of these tools have the capability of either internally calculating a wake structure or allowing for the prescription of a wake in the analysis. The influence of this wake structure is used in the induced-flow calculation process instead of the more simplified inflow assumptions.

The wake methods in use have had varying degrees of validation success, mostly compared with the only global data available—blade-tip-vortex trajectories—obtained by using flow-visualization techniques. (See ref. 4.) The results of these validation attempts have been encouraging. These wake methods are typically used in more complex rotor performance tools, primarily in the definition of the induced flow to the rotor system. Therefore, it seems that a prudent validation would be to examine the ability of the wake method to accurately compute

the induced velocity above the rotor. The availability of the nonintrusive laser velocimeter measurement technique makes it possible to obtain the necessary measurements just above the rotor system for this validation process.

The purpose of this study was to document some of the results of a continuing program of the Army Aerostuctures Directorate at Langley Research Center (LaRC) with code validation as a major goal. The results presented in this study are only a small portion of the data acquired above a research rotor and represent the induced-velocity characteristics for this rotor at 3 advance ratios—0.15, 0.23, and 0.30. These measurements were made on a four-bladed, rectangular-planform, articulated rotor system operating at representative tip Mach numbers and thrust levels. The data presented are the time-averaged and time-dependent measurements acquired from references 5 to 7.

These data have been compared with the induced-velocity calculations obtained using the free-wake option (ref. 2) of the Comprehensive Analytical Model of Rotorcraft Aerodynamics and Dynamics (CAMRAD)—commonly referred to as the "Scully Wake." (See ref. 8.) CAMRAD allows the user to selectively determine the method of rotor-performance trim option. This report documents the effect of the selection of two of these trim options.

Symbols

A	rotor disc area, πR^2
C_T	rotor thrust coefficient, $T/(\rho A V_T^2)$
q	free-stream dynamic pressure, $1/2 \rho V_\infty^2$, lbf/ft ²
r	local radius of rotor system, ft
R	rotor radius, ft
T	thrust produced by rotor, lbf
x	rotor propulsive force, lbf
v	local velocity measured normal to rotor tip-path plane (positive up), ft/sec
V_∞	free-stream velocity, ft/sec
V_T	rotor-blade-tip velocity ΩR , ft/sec
α_s	angle between rotor disk and free-stream velocity (positive nose up), deg
λ_i	induced-inflow ratio, $\lambda_i = (v + V_\infty \sin(\alpha_s))/V_T$ (positive up)
μ	rotor advance ratio, $(V_\infty \cos(\alpha_s))/V_T$

Ω	rotor rotational speed, rad/sec
Ψ	rotor azimuth measured from downstream position (positive counterclockwise) as viewed from above, deg
ρ	air density, slug/ft ³

Experimental Apparatus

The experimental apparatus used in this investigation included the Langley 14- by 22-Foot Subsonic Tunnel, the 2-meter rotor test system (2MRTS), and a 2-component laser velocimeter system (LV). The 2MRTS is a general-purpose rotorcraft model system mounted on a strut in the forward part of the test section of the 14- by 22-Foot Subsonic Tunnel. (See fig. 1.) The system consists of a 29-hp electric-drive motor, a 90° speed-reducing transmission, a blade-pitch control system, and two, six-component strain-gage balances used to provide independent measurement of forces and moments on the rotor system and fuselage shell. The four-bladed rotor hub is fully articulated with viscous dampers for lead-lag motion and coincident flap and lag hinges. More detailed descriptions of the 2MRTS and the fuselage are contained in reference 9. The blades used for these tests were of rectangular planform, NACA 0012 airfoil distribution, linear -8° twist, 33.88-in. radius, and 2.6-in. chord. (See ref. 5.) No attempt was made to dynamically scale these rotor blades; rather, they were very rigid, which reduced the uncertainty in the results caused by dynamic twisting of the blades.

The LV system used in this investigation was capable of measuring the instantaneous components of velocity in the longitudinal (free stream) and vertical directions. It is described in detail in each of the data references (refs. 5 to 7) and includes four subsystems: optics, traversing, data acquisition, and seeding. The optics subsystem operated in back-scatter mode and at high power (4 W in all lines) to accommodate the long focal lengths needed to scan the wide test section. The traverse subsystem provided 5 degrees of freedom (streamwise, vertical, lateral, pan, and tilt) in positioning the measurement location (sample volume) and was controlled by the same computer that was used for data acquisition. For this study, the traversing system was positioned to the right of the test section when looking upstream. The data-acquisition subsystem interfaced with the optical signal-processing equipment to receive two channels of raw LV data and up to five channels of coincident auxiliary data. In this investigation, four of the auxiliary channels were used for the acquisition of blade position. Two of the channels

(one each for the velocity components) measured the azimuthal position of the rotor shaft, and the other two measured lead-lag and flapping motion. This system converted the raw LV data to engineering units and determined the statistical characteristics of the acquired data so that the test results could be evaluated during the acquisition process. The raw data, the data which had been converted to engineering units, and 64 parameters from the tunnel static data-acquisition system were written to magnetic tape for later analysis. The final function performed by the data system was to control the five-degree-of-freedom traversing system. The seeding subsystem was a solid-particle, liquid-dispensing system. (See refs. 10 and 11.) The particles used in this investigation were polystyrene and were 1.7 μm in diameter. The advantages of the polystyrene particles were their low density, high reflectivity, and precise particle size.

Test Procedures

In all cases, measurements were made at azimuthal increments of 30° from $\Psi = 0^\circ$ at 3.0 in. (approximately one chord) above the plane formed by the tips of the blades. Measurements were made from radial locations of $r/R = 0.2$ to $r/R = 1.10$, and the majority of the measurement locations were concentrated toward the outboard portion of the disk. (See fig. 2.) During the test, the rotor-shaft angle of attack was maintained at -3° relative to the free stream for the advance-ratio data of 0.15 and 0.23, and at -4° for the advance-ratio data of 0.30. When longitudinal and lateral flapping relative to the shaft were maintained at zero, the performance measurements indicated that these shaft angles resulted in zero propulsive force at these three advance ratios. The operating tip speed for the test was held at 624 ft/sec (2113 rpm), and the nominal rotor thrust coefficient was held at 0.0064. Further details of the test operating conditions are contained in references 5 to 7. The LV data-acquisition process consisted of placing the sample volume at the measurement location and acquiring the conditionally sampled data for a period of 2 min, or until 4096 individual particle velocity measurements were made in either the longitudinal or the vertical component. Each of the individual particle velocity measurements in each component were associated with a number that represented the blade azimuth position at the time of the measurement. At the conclusion of the process, the measurement location was changed and the acquisition process was repeated.

Analytical Method

Even though a stand alone version of the free-wake module incorporated within CAMRAD was

available, the CAMRAD analysis was utilized for the calculations presented herein. The complete analysis was used because of the ability to evaluate the effects of several rotor-system parameters unique to this method, such as blade torsional stiffness, blade mass distribution, lead-lag hinge stiffness and damping characteristics, and control-system stiffness characteristics. Also, the ability to incorporate the inflow solution from a selected wake geometry within the rotor trim solution was considered to be important.

The only wake geometry option selected for analysis with the CAMRAD methodology was the free-wake model developed by Scully (ref. 8). The method, fully described in references 2 and 8, consists of line segments for the tip vortices and an option of rectangular sheets or line segments for the inboard shed and trailed-wake vorticity. For the analyses presented, the inboard shed and trailed-wake vorticity were modeled as line segments. Only the geometry of the rolled-up tip vortices (in this case selected to include all trailing vortices outboard of 80-percent span) was allowed to distort in the full relaxation technique. A rigid geometry was used for all the inboard vorticity.

The calculation of the wake geometry incorporates an efficiency procedure that utilizes a near-wake and far-wake scheme. At any given time in the wake geometry calculation, a boundary exists between the distorted wake and the initial rigid wake. Accounting for the induced effects from the far wake at the boundary in the near-wake calculations and updating the boundary conditions on a limited but regular basis was effective in reducing the computation time and providing reasonable accuracy and convergence.

The two trim options utilized in this analysis included:

1. trimming thrust coefficient to that set in the wind-tunnel experiment by using the rotor collective. Rotor longitudinal and lateral cyclics and shaft angle of attack were set to those used in the experiment.

2. trimming lift coefficient, longitudinal and lateral flapping angles, and propulsive force coefficient by using collective, rotor longitudinal and lateral cyclics, and shaft angle of attack.

In the present modeling process, the calculations were very sensitive to the lead-lag hinge stiffness and damping characteristics parameters. Accounting for these and trimming the rotor system to the desired values of C_T and longitudinal and lateral flapping, the calculated cyclic control angles were close to the values measured in the wind tunnel. This experience provided confidence in the selection of the structural properties to be included in the calculations for the off-rotor, field-point induced velocities. Be-

cause of these preliminary calculations, trim option 1 trimmed only to thrust coefficient. The experimentally measured cyclic controls and angle of attack were used, and the resulting blade-motion calculations were checked to be consistent with those measured (zero longitudinal and lateral flapping). For trim option 2, trimming included all the parameters mentioned above.

The calculations presented in this paper were all made on a DEC VAX 11/780 and two MicroVAX II computer systems. The field velocity calculations were made in a plane off the rotor disc identical with the plane measured in the laser velocimeter experiments. Some of the critical parameters used in the rotor aerodynamic modeling were

1. 9 radial aerodynamic segments with edges at $r/R = 0.246, 0.45, 0.55, 0.6625, 0.7375, 0.8, 0.85, 0.9, 0.95, \text{ and } 1.0$
2. 0.97 tip-loss factor
3. uniform radial distribution of blade mass, chordwise bending stiffness, flapwise bending stiffness, and torsional stiffness
4. static stall model
5. NACA 0012 low Reynolds number airfoil data tables used

Some of the critical parameters used in the "Scully Wake" model were

1. 3 wake geometry iterations
2. 0.0025 r/R tip vortex core radii
3. vortex core bursting suppressed
4. all vortices defined with line segments of linear circulation distribution
5. wake extent definition was: Near wake = 6, Far wake = 12, and Far wake for field-point velocity calculations = 96

Results and Discussion

Experimental Results

The average induced-inflow-ratio data measured above the rotor system for advance ratios of 0.15, 0.23, and 0.30 are presented in contour format in figure 3. The view in figure 3 is as if the reader were above the rotor looking down on the rotor disc. The free-stream direction is from left to right, and the direction of rotor rotation is counterclockwise. Two circles are evident in each part of figure 3—the inboard radius, where the innermost measurements were acquired, and the path of the tip of the rotor blades. The data presented in figure 3 are shown as regions of induced-inflow ratio represented by different colors. For instance, in figure 3(a) induced-inflow-ratio

values between 0 and -0.01 are represented by the color blue. The induced-inflow ratio is defined as

$$\lambda_i = (v + V_\infty \sin(\alpha_s))/V_T$$

where v is the component of the measured induced-velocity vector that has been resolved normal to the rotor tip-path plane. The maximum and minimum values of measured induced inflow are listed at the bottom of each figure on either end of the color bar.

The zero-velocity line is important on each contour plot and is consistently indicated as the border between the colors blue and brown. The results at all three advance-ratio conditions indicate that the induced flow to this rotor system is not symmetrical about the longitudinal centerline of the rotor and that the greatest downwash occurs in the rear portion of the disc and is skewed to the advancing side. The extent of the induced-upflow region moves progressively from the forward portion of the disc at $\mu = 0.15$, where it encompasses only 20 percent of the disc, to a point where it covers most of the forward half of the disc at $\mu = 0.30$. The presence of the concentrated tip vortices and rollup of the wake structure are indicated in the $\mu = 0.15$ data on both sides of the rotor disc, where the contours are tightly spaced; these factors are indications of large velocity gradients. However, as the advance ratio is increased, the evidence of the rollup process moves farther downstream, and the influence of the local induced velocities is less. At $\mu = 0.30$, the contours on the advancing side of the rotor do not indicate the strong velocity gradients that existed at $\mu = 0.15$.

Analytical Comparisons

The induced-inflow calculations from CAMRAD using trim option 1 (trimming only to C_T and using the experimental values of rotor cyclics and shaft angle of attack) were already available in reference 12. However, the results of that analysis raised questions as to the accuracy of the analytical procedure for computing the induced-inflow characteristics based on setting the shaft angle of attack to the experimental value. Therefore, trim option 2 in CAMRAD was used to evaluate the effect of trimming the rotor to the correct propulsive-force coefficient. In the experiment, the rotor-system propulsive force was set to 0.0; however, this measurement included the drag forces produced by all the rotating components, such as the rotor blades, hub, shaft, and push rods (not the fuselage). Since CAMRAD does not model all these components (notably the hub, shaft, and push rods), it was necessary to estimate the propulsive force required to overcome the parasitic drag of these elements. To accomplish this, CAMRAD was exercised

at several levels of propulsive force, and these performance predictions were compared with the results of the experiment at the three advance ratios tested.

The results of these calculations are presented in figure 4 for a range of frontal flat-plate area estimates x/q from 0 to 0.4. Presented in the results are the predictions for horsepower, shaft angle of attack, rotor collective, rotor longitudinal cyclic, and rotor lateral cyclic (figs. 4(a) to 4(e)). The experimentally determined values are also presented in each figure. It is evident from figure 4(a) that the required horsepower predicted by CAMRAD by using the experimental shaft angle of attack does not represent the horsepower used in the experiment. The frontal flat-plate area most appropriate for these calculations should be $x/q = 0.2$. Calculations of the shaft angle of attack, rotor collective, and rotor lateral cyclic (figs. 4(b), 4(c), and 4(e)) are inconclusive in determining the required frontal area. Longitudinal-cyclic calculations (fig. 4(d)) indicate that the appropriate trim calculations should either be set at the experimental shaft angle of attack or trimmed to $x/q = 0.2$. As expected, the rotor-shaft angle of attack required to trim the rotor to zero propulsive force changes at each advance ratio. This is evident in the measured and predicted results. It should not be assumed that the frontal area of the parasitic-drag components would remain constant for each of these angles at the different advance ratios; however, to evaluate the effect of this particular trimming option, it was decided that trimming to a propulsive force of 0.2 would be most effective.

The results of the analytical calculations for trim options 1 and 2 are presented in figures 5(a) and (b) for $\mu = 0.15$, in figures 6(a) and (b) for $\mu = 0.23$, and in figures 7(a) and (b) for $\mu = 0.30$. The format is similar to that for the experimental contour plots of figure 3. Every effort was made to calculate contour levels, from the analytical results at each advance ratio, that were consistent with those calculated from experimental results. The inner circle represents the innermost portion of the disc for which calculations were made, and the black circle is the path of the tips. The view is again from above with the free stream from left to right. The direction of rotation is counterclockwise. The maximum and minimum values of induced inflow calculated are listed at the bottom of each figure on either end of the color bar.

When compared with the data presented in figure 3(a), the calculations presented in figures 5(a) and (b) at $\mu = 0.15$ show that the predictions also indicate a region of upflow over the front 20 percent of the rotor disc. The high gradients experienced, particularly on the advancing side of the rotor, are predicted by the method. One interesting detail in

Both trim-option calculations is that the maximum downwash is located on the retreating side of the rotor disc—just the opposite from what the experiment shows. As shown in figures 5(a) and (b), no appreciable difference can be seen between the results of the two trim-option calculations.

The results of the calculations at $\mu = 0.23$ (fig. 6) are similar to those at $\mu = 0.15$, but there are some notable exceptions. When compared with the experimental data of figure 3(b), it is evident that the extent of the induced upflow at $\mu = 0.23$ was not modeled well by either of the trim-option methods used. Even though the experimental data show weaker gradients on either side of the rotor at $\mu = 0.23$ than at $\mu = 0.15$, the rollup process is still indicated and modeled to some degree by both of the trim-option methods.

The results for the predictions at $\mu = 0.30$ are presented in figure 7 and are similar to those at $\mu = 0.23$. The method fails to model the extent of induced upflow as measured in the experiment (fig. 3(c)). The effect of trimming the rotor to an appropriate propulsive force does not provide for a modeling to the extent of upflow that was hoped. The analysis again indicates that the maximum downwash occurs on the retreating-blade side of the rotor disc—opposite from that measured (fig. 3(c)).

These detailed differences seem significant, but when considering the implications of the application of the analyses, it is important to determine the relative effects of the inability of the analysis in the prediction process. One of the uses for the wake methods is to calculate the induced velocities, and thus the local blade angle of attack, in the process of computing the blade load distribution and rotor performance. In the rotor environment, it is difficult to measure the local rotor-blade angle of attack. To provide a relative measure of the errors involved in the predicted calculations for angle of attack, the differences between the wake calculations and the data were used only with the free-stream velocity and rotor rotational velocity to compute the error in the methods of predicting the local mean-flow angle. Emphasis must be placed on the word "relative," because these numbers should not be taken as an absolute representation of the angle-of-attack distribution for the rotor blades; the measurements in the rotor environment are never free of the induced effect of the lifting blades. Only the normal component of induced velocity, rotor rotational velocity, and free-stream velocity are used in these simple calculations.

The data presented in figures 8, 9, and 10 are the distributions of the calculated relative difference in flow angle computed from the experimental data

and that computed by each analysis. The figures are similar to the other color contour plots, but each color represents a region of calculated angle between two limits. For instance, all calculated angles in figure 8(a) between 0° and 1° are shown in yellow. Again, the calculations do not include any induced-velocity components other than those measured or calculated normal to the rotor tip-path plane. Because of the relatively low local rotational velocity at the inner part of the rotor, and because of the effects of the hub and fuselage (which are not modeled in the theory), the difference in flow-angle calculations tends to be larger near the tips; this difference is not necessarily caused by the fact that the difference in calculating induced velocities is greater. The difference becomes more apparent near the region of reversed velocities near the hub on the retreating-blade side of the hub.

This relative difference in mean-flow angle for most of the test conditions is between -1° and $+1^\circ$; that is, the error in the calculation of rotor-blade angle of attack may be no more than 1° . Even though this can be significant, depending on the local onset flow velocity, in predicting a thrust distribution over the rotor disc, regions of larger flow-angle difference are of more concern. In the first quadrant (advancing-blade side), the larger negative flow-angle differences are the direct result of the inability of the analysis to compute the degree of downwash on this side of the rotor. However, the greatest concern is for the region where the flow-angle error is greater than 1° . At an advance ratio of 0.15 (figs. 8(a) and 8(b)) this region is relatively small, but as the advance ratio increases to 0.23 and 0.30, this region grows to an area that encompasses a large percentage of the third quadrant of the rotor disc (figs. 9 and 10). In these calculations, the method used for trim had very little effect on the overall results of the comparisons of measurement versus analysis.

Time Dependent Induced Inflow

At each of the 180 measurement locations at each advance-ratio condition tested, data were conditionally sampled with rotor-blade position. These data were sorted in "bins" of constant azimuth width, and the statistical mean was calculated in each bin. Instead of presenting all 540 time-dependent plots and corresponding CAMRAD predictions available in the data base, selected samples of these are presented in time-history format in figures 11 to 13. A measure of the unsteady time-dependent flow is provided by calculating the order ratio analysis of each of the time-history measurements and CAMRAD calculations and selecting the blade-passage order (the frequency corresponding to 4 times the rotational

frequency). An order-ratio analysis of a sample inflow measurement at a selected location is provided in figure 14. These numbers were all collected and presented in figures 15 and 16 as the distribution of the fourth harmonic of the oscillatory induced-inflow ratio.

The data presented in figures 11 to 13 represent selected time histories at advance ratios of 0.15 (150° azimuth), 0.23 (330° azimuth), and 0.30 (180° azimuth), respectively. Part (a) of each figure is an example of a comparison of the measurement with the two CAMRAD trim-option calculations at a measurement location near the root of the rotor blade; part (b) of each figure is an example of such a comparison at a measurement location near the tip of the rotor blade. The induced-inflow ratio plotted as a function of the position of the number-1 blade (reference blade) at the instant the measurement was made is shown in each portion of each figure. The most obvious difference between the measurements and the CAMRAD predictions is the resolution in azimuth. The measurement resolution was 2.81°, and the CAMRAD prediction resolution was 15°. This was the maximum resolution available in this version of CAMRAD using the free-wake option. The limitations in the CAMRAD prediction resolution resulted in a considerable degradation of the inflow waveform compared with the measured data.

For an advance ratio of 0.15 (fig. 11), the peak-to-peak variation of induced inflow at $r/R = 0.4$ (fig. 11(a)) was not modeled well with the CAMRAD predictions; however, near the tip at $r/R = 0.9$, the waveform was modeled well by both CAMRAD trim-option calculations if the limitations in azimuth resolution in the CAMRAD calculations are considered. The second trim option did increase the peak-to-peak oscillatory inflow prediction at the inboard radial positions, but not to the level of the measured peak-to-peak oscillatory inflow (fig. 11(a)). It is important to recognize that the resolution limitations of CAMRAD do not capture the high gradients measured near 60° azimuth, particularly near the rotor-blade tip. Similar conclusions can be drawn from the data presented for advance ratios of 0.23 and 0.30. As mentioned previously, 540 of these comparisons can be presented, but another method of presenting a global description of these oscillatory induced-inflow-ratio comparisons is required. To accomplish this comparison, the shaft-order, conditionally sampled, amplitude spectrum was computed at each of the 180 measurement locations. From these spectra, the fourth harmonic (blade-passage frequency) was chosen to be representative of oscillatory characteristics. This fourth-harmonic amplitude value was col-

lected for all measurement locations and is presented in contour format in figures 15 and 16.

Figure 15 provides this fourth harmonic of the order-ratio analysis of the measured induced-inflow ratio for the test-condition advance ratios of 0.15, 0.23, and 0.30. These comparisons can obviously be extended for other harmonics; however, a comparison with the CAMRAD analysis for the fourth harmonic is sufficient for the purposes of this analysis. Figure 16 presents these calculations for the CAMRAD analyses for trim option 1 at advance ratios of 0.15, 0.23, and 0.30. Considering the limited improvements obtained by trim option 2 and a careful review of the results of these calculations using this trim option, these results are not presented. The format of figures 15 and 16 are similar to the contour plots already presented for the distribution of induced-inflow ratio.

The experimental data presented in figure 15 show that the oscillatory inflow characteristics are at a maximum on the retreating-blade side of the rotor disc. The maximum oscillatory inflow occurs in the third quadrant between 180° and 270° azimuth, particularly at an advance ratio of 0.30. For all rotor-test conditions, the oscillatory inflow on the advancing-blade side of the rotor disc is minimum. The data presented in figure 15(a) show a large oscillatory inflow in the fourth and third quadrants. This can also be seen at the higher advance ratio, but not at the same high levels evident in figure 15(a).

The analytical predictions of oscillatory induced-inflow ratio are presented in figure 16 and indicate an important similarity to the experimental data. Considering that the oscillatory inflow characteristics presented in these figures are directly related to the effect of the blade passage, it is hoped that the analysis would reproduce the effects of the disturbance of the passage of the lifting body. However, considering the inability of the method to compute the average inflow effects and the implications of this deficiency in the prediction of angle of attack and resulting spanwise and azimuthally dependent blade-load distribution, it is surprising that the trends evident in the oscillatory induced calculations are so similar to the experimentally measured values. At all advance ratios, the maximum oscillatory inflow is in the third quadrant, but at slightly higher values than those measured. The large oscillatory inflow evident in the experimental data in the fourth quadrant is also present in the analytical predictions. The size of the maximum oscillatory inflow for the analytical results is much larger than those measured, particularly at an advance ratio of 0.23 (figs. 15(b) and 16(b)). The contours shown for the analytical

results are much smoother than those measured, probably because the measurements are affected by blade-to-blade variability, whereas the predictions assume that the results of each blade passage is identical to the other three. The effects of the high-gradient inflow characteristics on the measured data are not shown here, because the contours are presented only for the fourth harmonic (or blade-passage frequency). The results from the predictions using trim option 2 are not shown, because the results do not contribute to those conclusions already obtained.

Concluding Remarks

A comparison between CAMRAD (Comprehensive Analytical Model of Rotorcraft Aerodynamics and Dynamics) and rotor inflow measurements using a laser velocimeter has been presented. The results are presented for a four-bladed rotor system, with rectangular blade planform, operating at a thrust coefficient of 0.0064. The measurements were obtained at azimuthal increments of 30°, 3.0 in. above the plane formed by the tips of the blades at radial locations ranging from 20 percent to 110 percent of the span. The measurements included time-averaged induced-inflow characteristics and conditionally sampled data. The model used in the CAMRAD code utilized the "Scully Free-Wake" option. Two rotor-trim options were used in the analysis. The results observed from the experimental measurements included:

1. As the advance ratio was increased, the region of average induced upflow progressively moved from the forward 20 percent of the rotor disc to most of the front half of the rotor disc.
2. The maximum downwash occurred in the rear portion of the rotor disc and skewed to the advancing-blade side of the disc.

Comparison of the analytical method CAMRAD with the measurements resulted in the following conclusions:

1. The amount of average induced upflow was effectively modeled only at the 0.15 advance ratio and was severely underpredicted at the higher advance ratios.
2. The maximum predicted downwash consistently occurred in the rear portion of the rotor disc and skewed to the retreating-blade side of the disc.
3. Using the trim option that computed trim based on rotor propulsive force did not affect these conclusions.

The evaluation of the ability of the method to calculate local rotor-blade angle of attack was done by

computing the effective mean-flow-angle error at the measurement location. The results were as follows:

1. Over most of the rotor disc at all three advance ratios, the error in this flow-angle correction was no more than 1°. However, because of the inability of the methods to predict the extent of the induced upflow (particularly at the higher advance ratios), there were large regions where this error in calculated flow angle was of concern from a performance-prediction standpoint.
2. Again, the trim-option selection was not critical in the calculations.

The comparison of the time-dependent characteristics of the measurements with those of CAMRAD showed that the high gradients evident in the measured results near blade passage were not at all captured by the analysis, particularly near the rotor-blade tip. The global indication of the time-dependent inflow as represented by the fourth harmonic of the order-ratio analyses of both the measured and predicted inflow suggested the following conclusions:

1. The maximum amplitude of the fourth-harmonic induced inflow occurred in the measurement and the analysis in the third quadrant of the rotor disc.
2. The size of this region was much larger for the analysis than was measured, particularly at the 0.23 advance ratio.

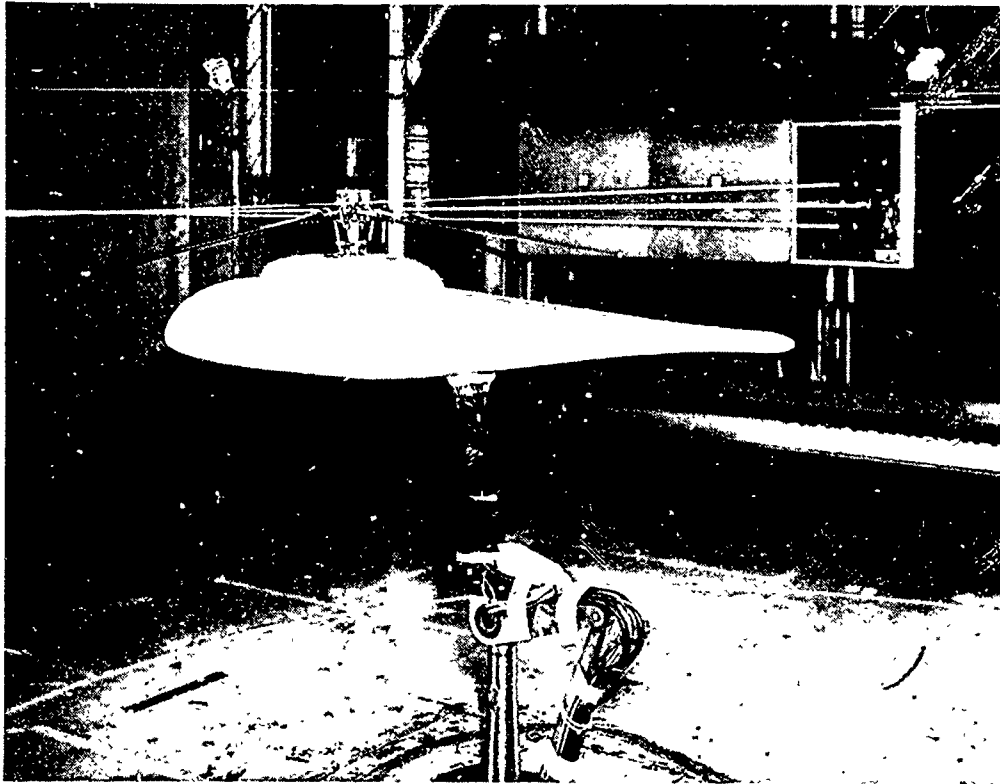
Generally, the analyses were deficient in the prediction of mean inflow characteristics at the higher advance ratios. Considering the implications of this deficiency related to angle of attack and resulting spanwise blade load distribution, it was surprising that the trends found in the oscillatory induced calculations were so similar to the measured values.

NASA Langley Research Center
Hampton, VA 23665-5225
October 10, 1989

References

1. Harris, Franklin D.: Rotary Wing Aerodynamics—Historical Perspective and Important Issues. Paper presented at the National Specialists' Meeting on Aerodynamics and Aeroacoustics, American Helicopter Soc., Southwest Region, Feb. 25-27, 1987.
2. Johnson, Wayne: *A Comprehensive Analytical Model of Rotorcraft Aerodynamics and Dynamics. Part I: Analysis Development*. NASA TM-81182, AVRADCOM TR-80-A-5, 1980.
3. Mangler, K. W.; and Squire, H. B.: *The Induced Velocity Field of a Rotor*. R. & M. No. 2642, British Aeronautical Research Council, May 1950.

4. Egolf, T. Alan; and Sparks, S. Patrick: *A Full Potential Flow Analysis With Realistic Wake Influence for Helicopter Rotor Airload Prediction*. NASA CR-4007, 1987.
5. Elliott, Joe W.; Althoff, Susan L.; and Sailey, Richard H.: *Inflow Measurement Made With a Laser Velocimeter on a Helicopter Model in Forward Flight. Volume I—Rectangular Planform Blades at an Advance Ratio of 0.15*. NASA TM-100541, AVSCOM TM-88-B-004, 1988.
6. Elliott, Joe W.; Althoff, Susan L.; and Sailey, Richard H.: *Inflow Measurement Made With a Laser Velocimeter on a Helicopter Model in Forward Flight. Volume II—Rectangular Planform Blades at an Advance Ratio of 0.23*. NASA TM-100542, AVSCOM TM-88-B-005, 1988.
7. Elliott, Joe W.; Althoff, Susan L.; and Sailey, Richard H.: *Inflow Measurement Made With a Laser Velocimeter on a Helicopter Model in Forward Flight. Volume III—Rectangular Planform Blades at an Advance Ratio of 0.30*. NASA TM-100543, AVSCOM TM-88-B-006, 1988.
8. Scully, M. P.: *Computation of Helicopter Rotor Wake Geometry and Its Influence on Rotor Harmonic Airloads*. ASRL TR 178-1 (Contracts N00019-73-C-0378 and N00019-74-C-0321), Massachusetts Inst. of Technology, Mar. 1975.
9. Phelps, Arthur E., III; and Berry, John D.: *Description of the U.S. Army Small-Scale 2-Meter Rotor Test System*. NASA TM-87762, AVSCOM TM 86-B-4, 1987.
10. Nichols, Cecil E., Jr.: *Preparation of Polystyrene Microspheres for Laser Velocimetry in Wind Tunnels*. NASA TM-89163, 1987.
11. Elliott, Joe W.; and Nichols, Cecil E.: *Seeding Systems for Use With a Laser Velocimeter in Large Scale Wind Tunnels. Wind Tunnel Seeding Systems for Laser Velocimeters*, William W. Hunter, Jr., and Cecil E. Nichols, Jr., compilers, NASA CP-2393, 1985, pp. 93-103.
12. Hoad, Danny R.; Althoff, Susan L.; and Elliott, Joe W.: *Rotor Inflow Variability With Advance Ratio. 44th Annual Forum Proceedings, American Helicopter Soc., c.1988, pp. 57-72.*



L-89-124

Figure 1. 2-meter rotor test system and laser-velocimeter system in Langley 14- by 22-Foot Subsonic Tunnel.

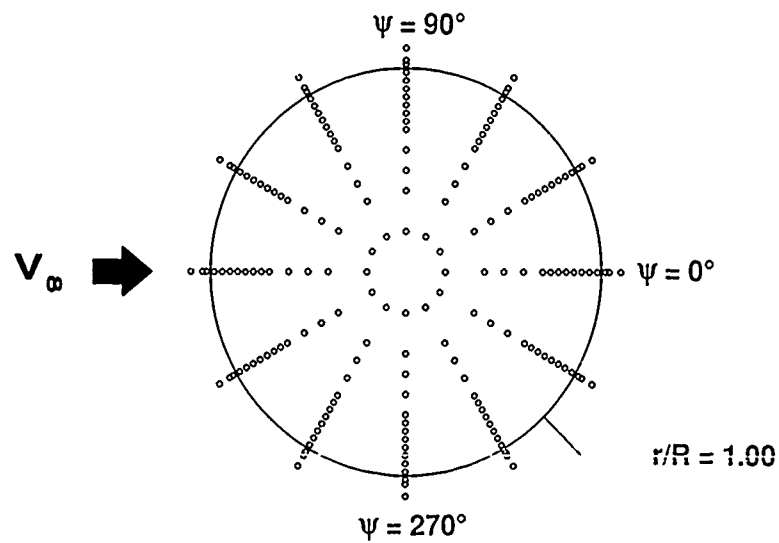
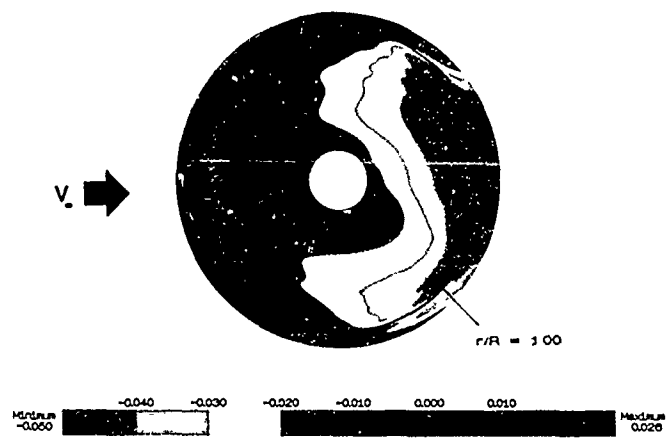
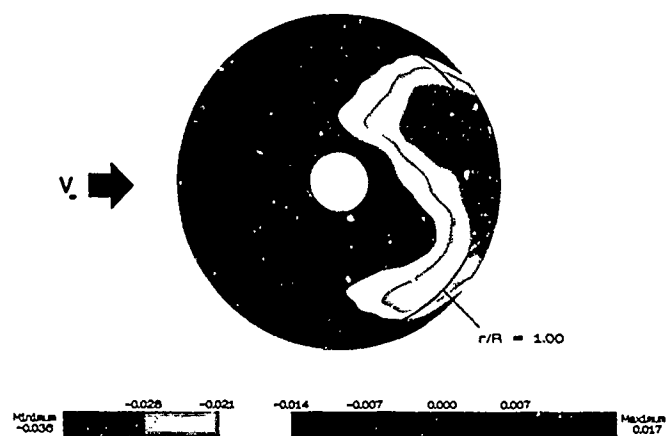


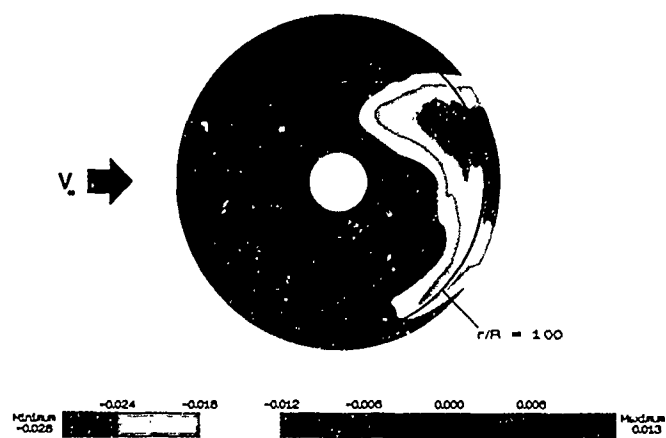
Figure 2. Location of velocity measurements 3.0 in. above rotor tip-path plane.



(a) $\mu = 0.15$; $\alpha_s = -3.0^\circ$.

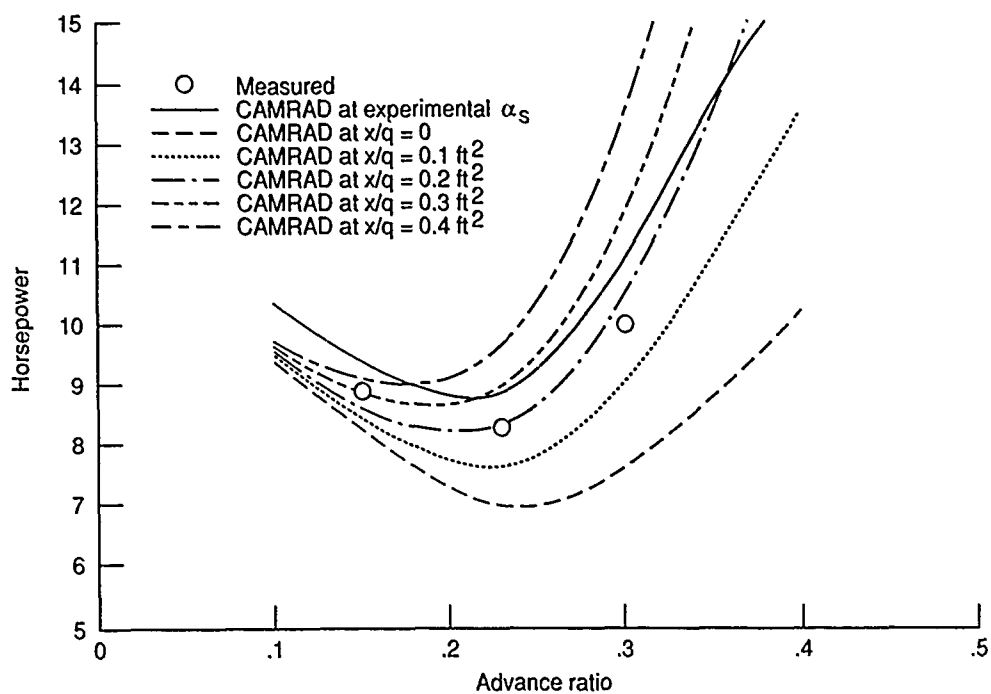


(b) $\mu = 0.23$; $\alpha_s = -3.0^\circ$.

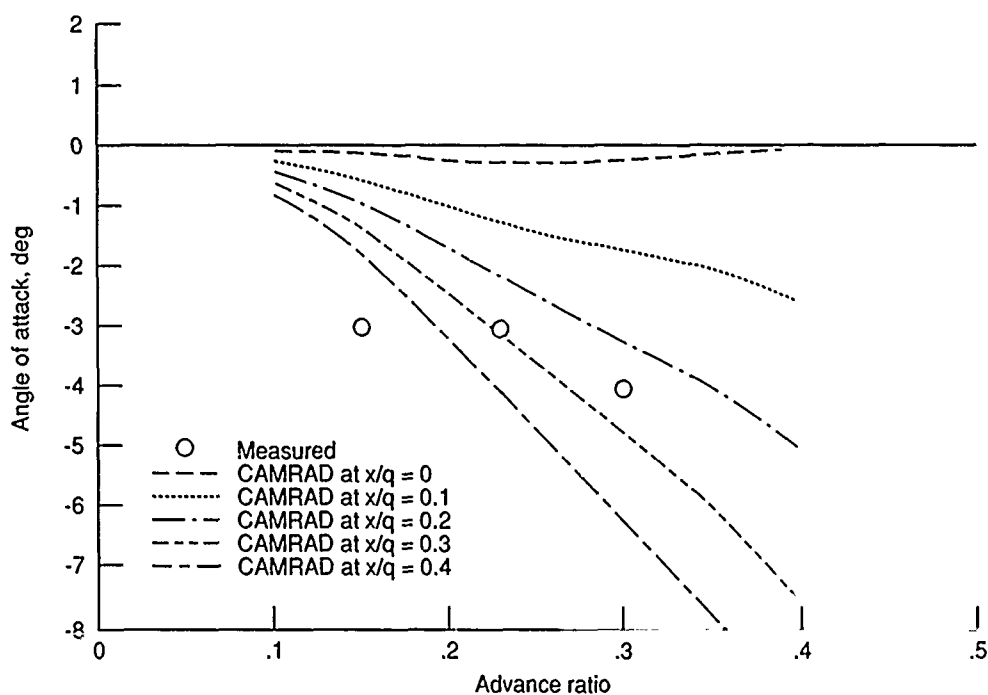


(c) $\mu = 0.30$; $\alpha_s = -4.0^\circ$.

Figure 3. Measured induced-inflow-ratio distribution 3 in. above rotor tip-path plane.

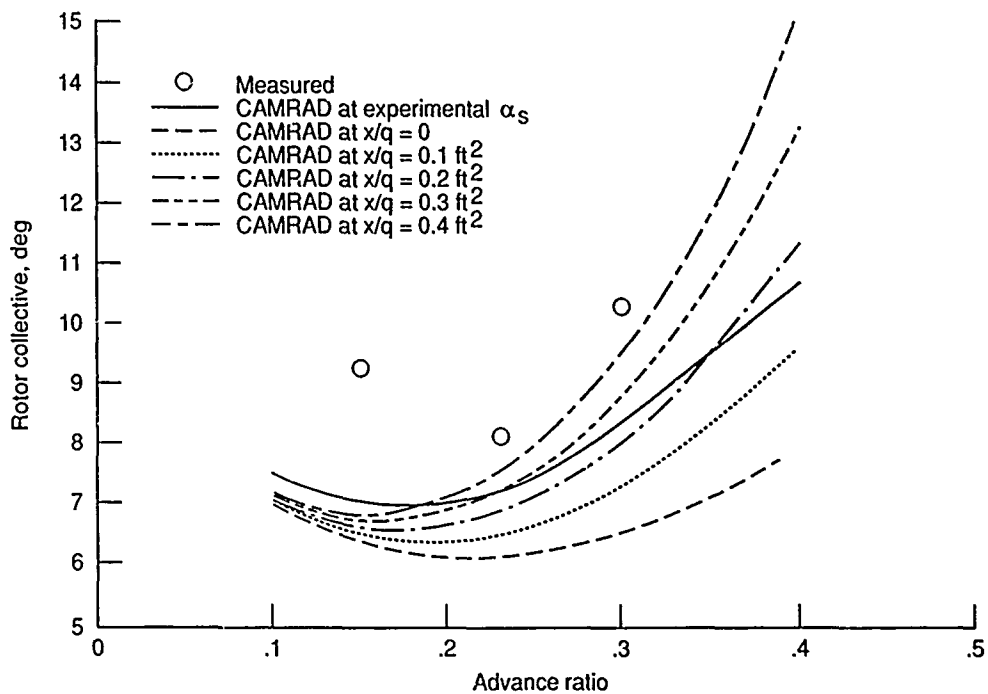


(a) Horsepower.

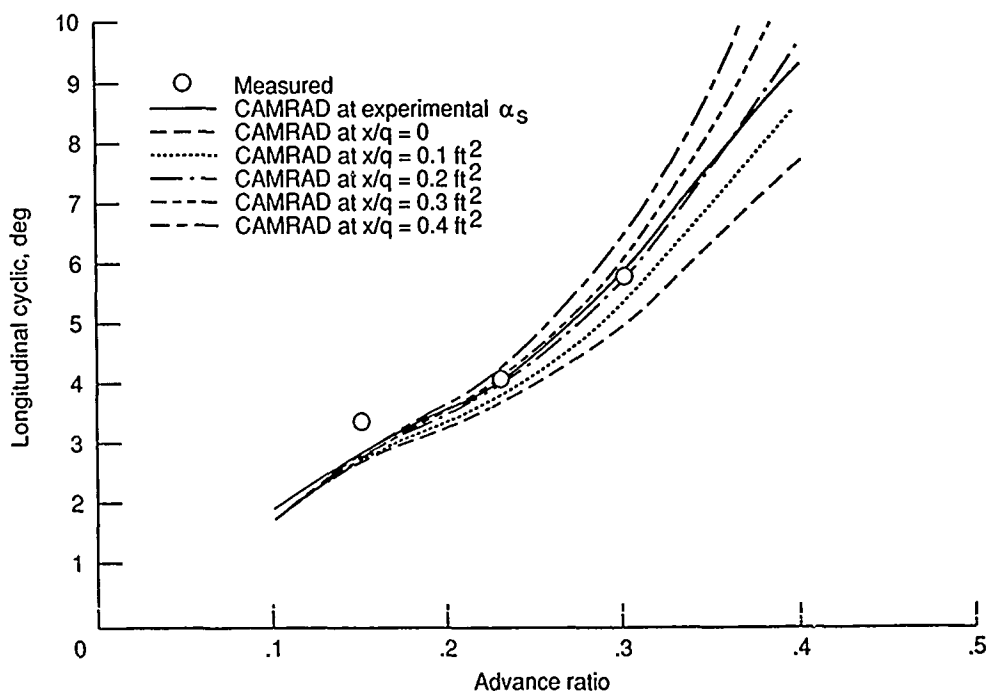


(b) Shaft angle of attack.

Figure 4. CAMRAD results at several values of propulsive force.

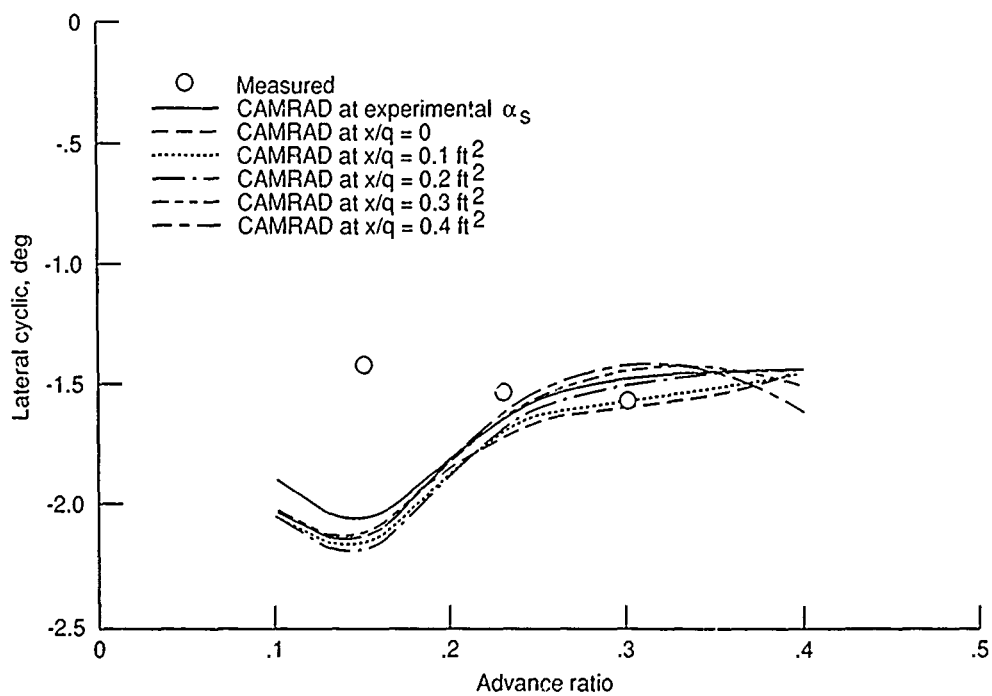


(c) Rotor collective.



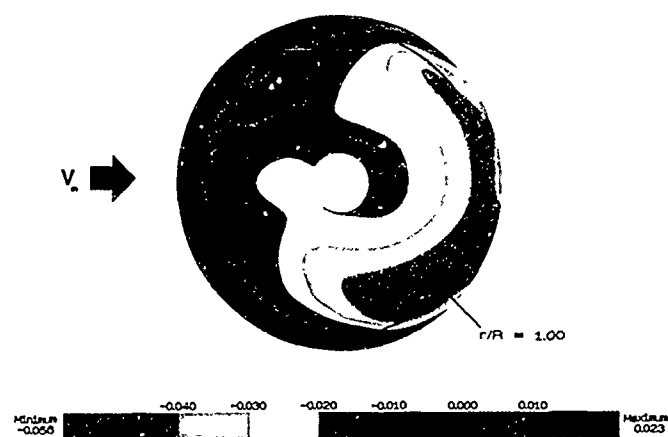
(d) Longitudinal cyclic.

Figure 4. Continued.

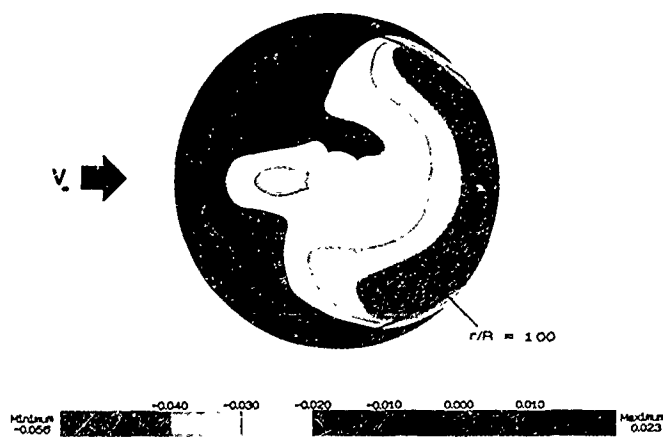


(e) Lateral cyclic.

Figure 4. Concluded.

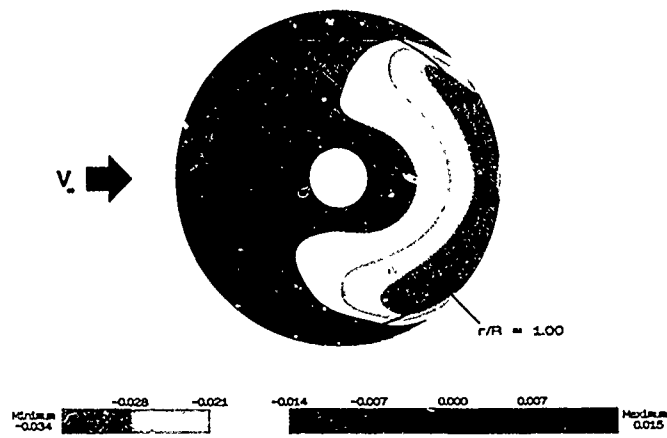


(a) Trim option 1.

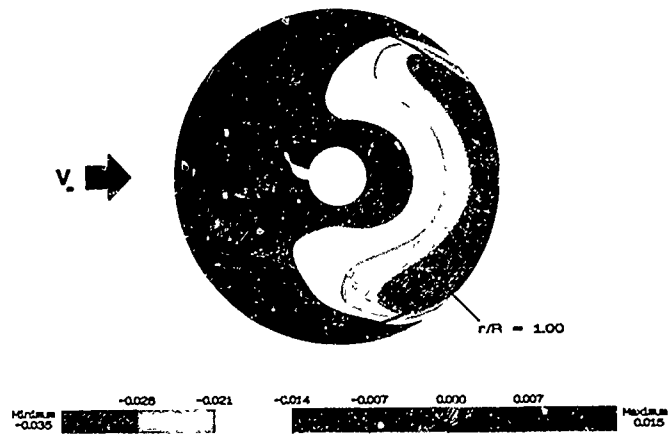


(b) Trim option 2.

Figure 5. CAMRAD predictions for induced-inflow-ratio distribution at $\mu = 0.15$.

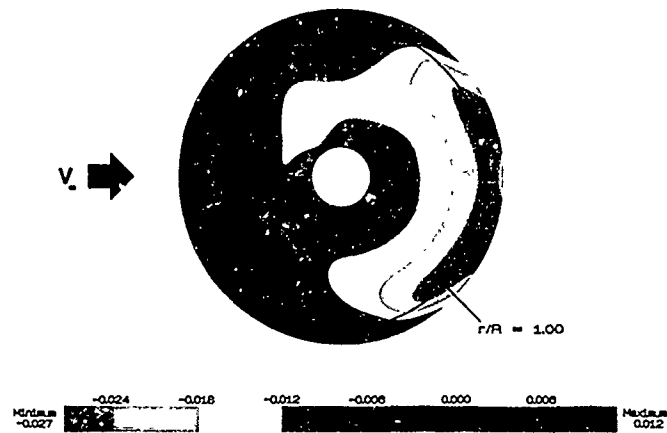


(a) Trim option 1.

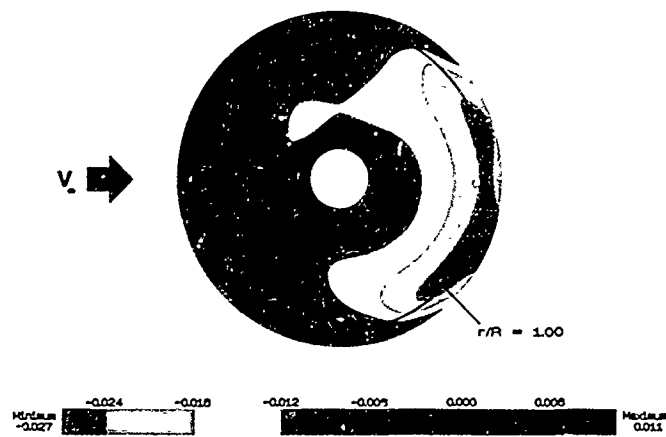


(b) Trim option 2.

Figure 6. CAMRAD predictions for induced-inflow-ratio distribution at $\mu = 0.23$.

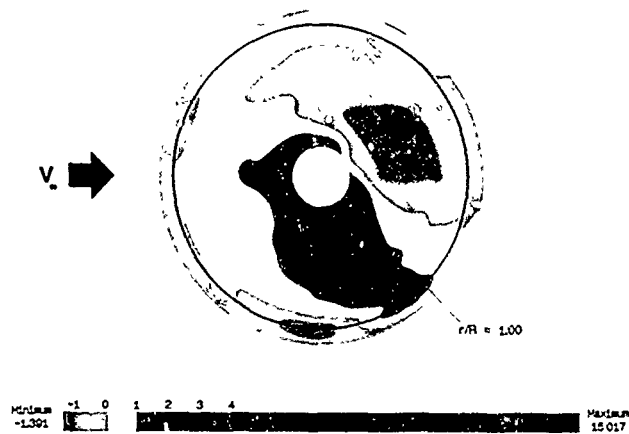


(a) Trim option 1.

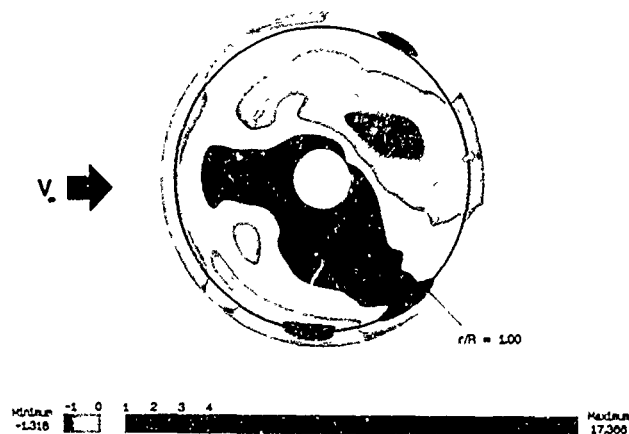


(b) Trim option 2.

Figure 7. CAMRAD predictions for induced-inflow-ratio distribution at $\mu = 0.30$.

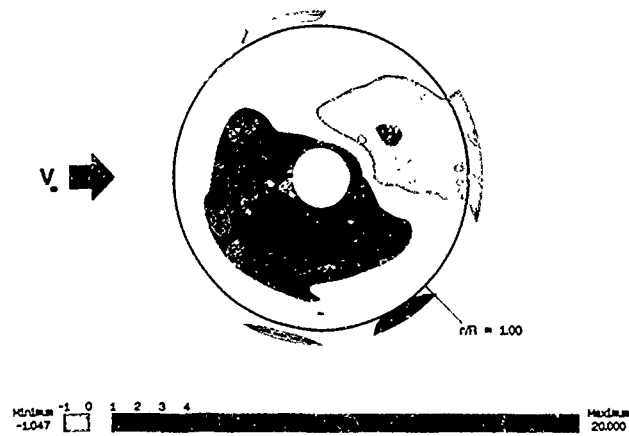


(a) Trim option 1.

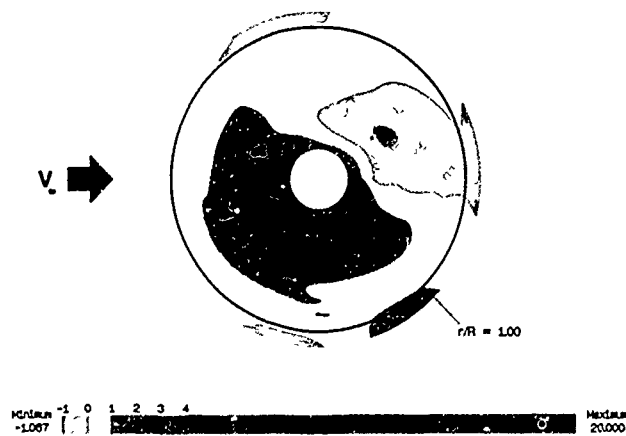


(b) Trim option 2.

Figure 8. Relative error in calculation of local flow angle above rotor system at $\mu = 0.15$.

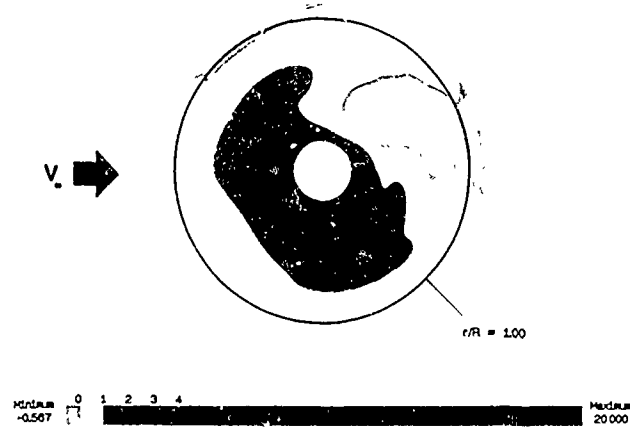


(a) Trim option 1.

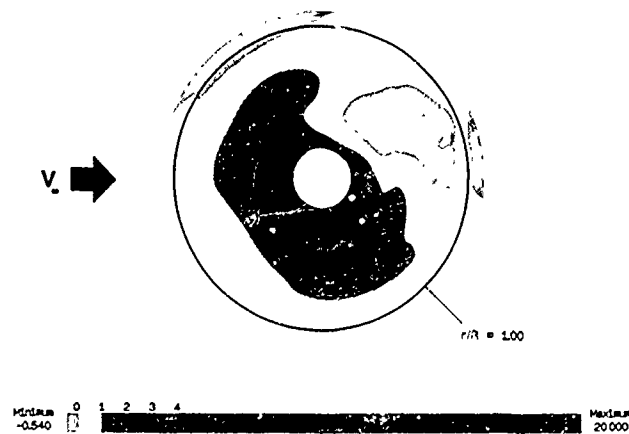


(b) Trim option 2.

Figure 9. Relative error in calculation of local flow angle above rotor system at $\mu = 0.23$.

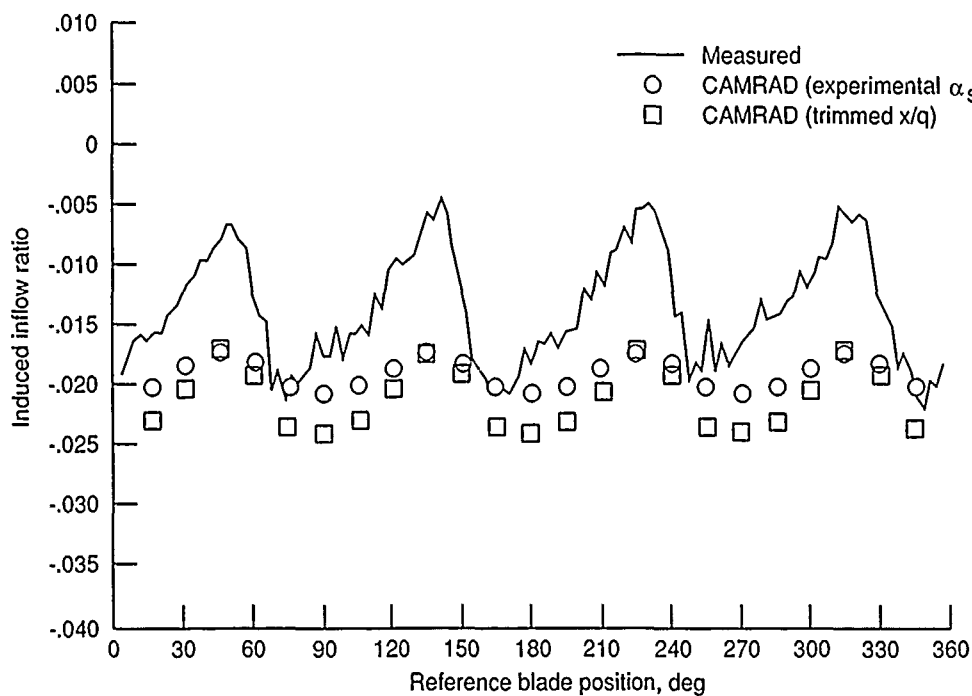


(a) Trim option 1.

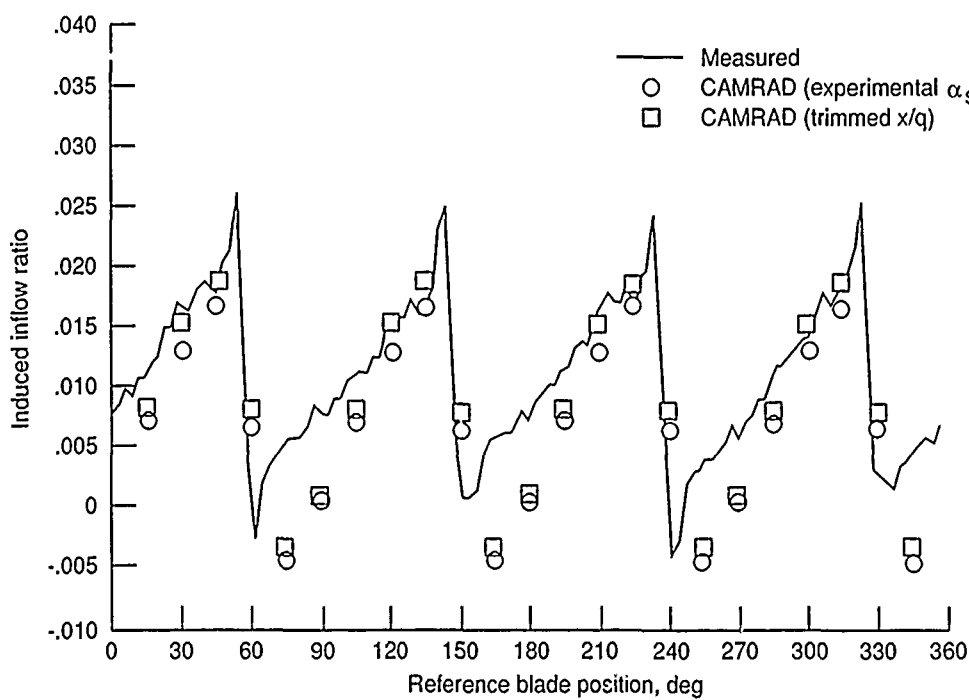


(b) Trim option 2.

Figure 10. Relative error in calculation of local flow angle above rotor system at $\mu = 0.30$.

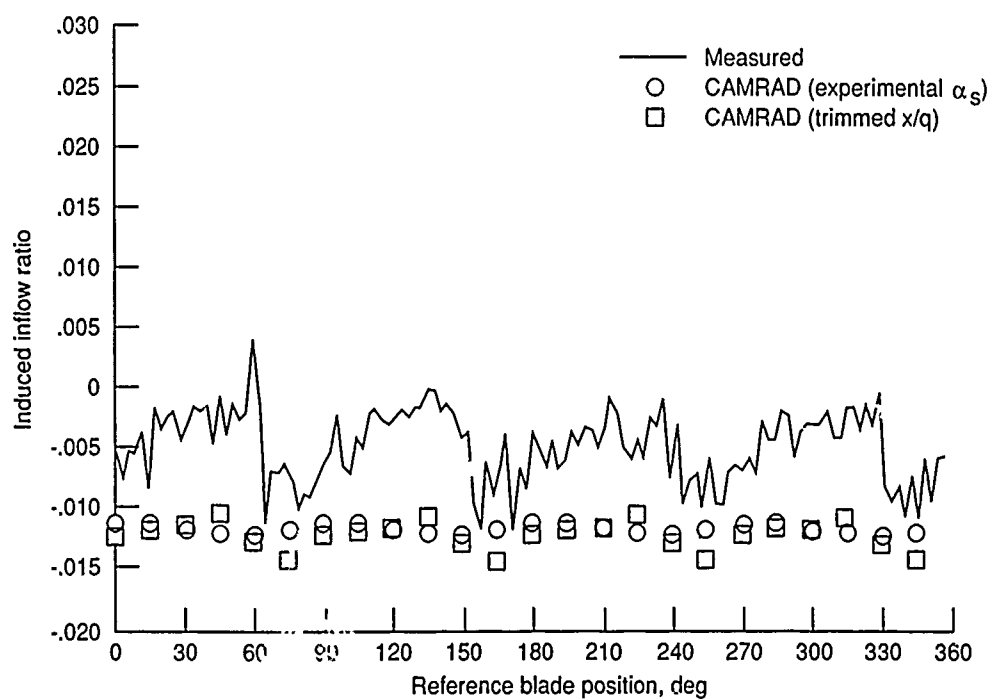


(a) $r/R = 0.40$.

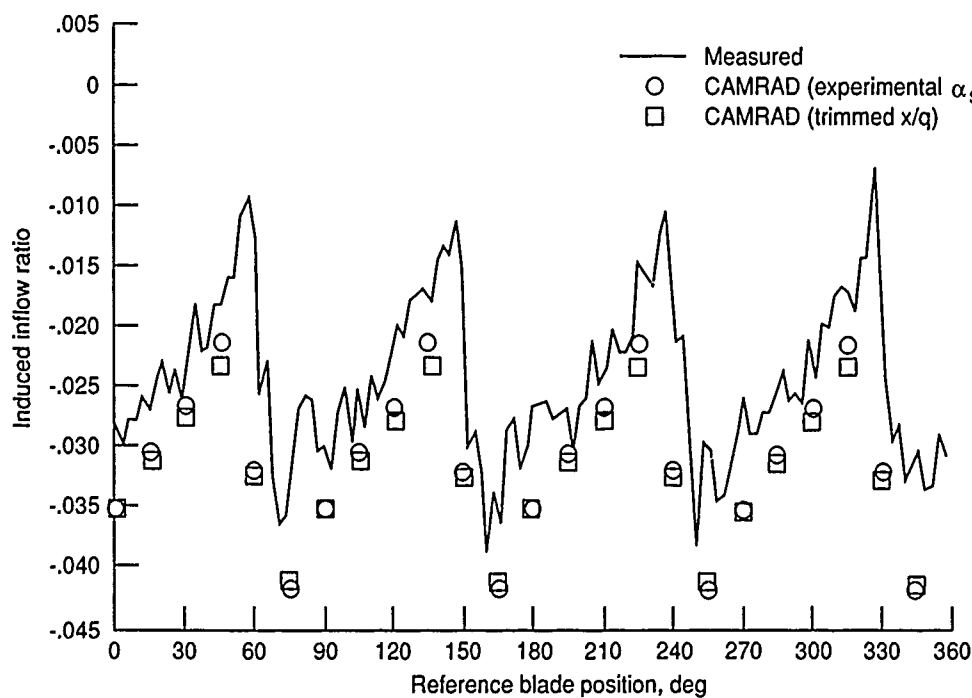


(b) $r/R = 0.90$.

Figure 11. Time history of measured and CAMRAD predicted induced-inflow ratio at $\mu = 0.15$ and 150° azimuth.

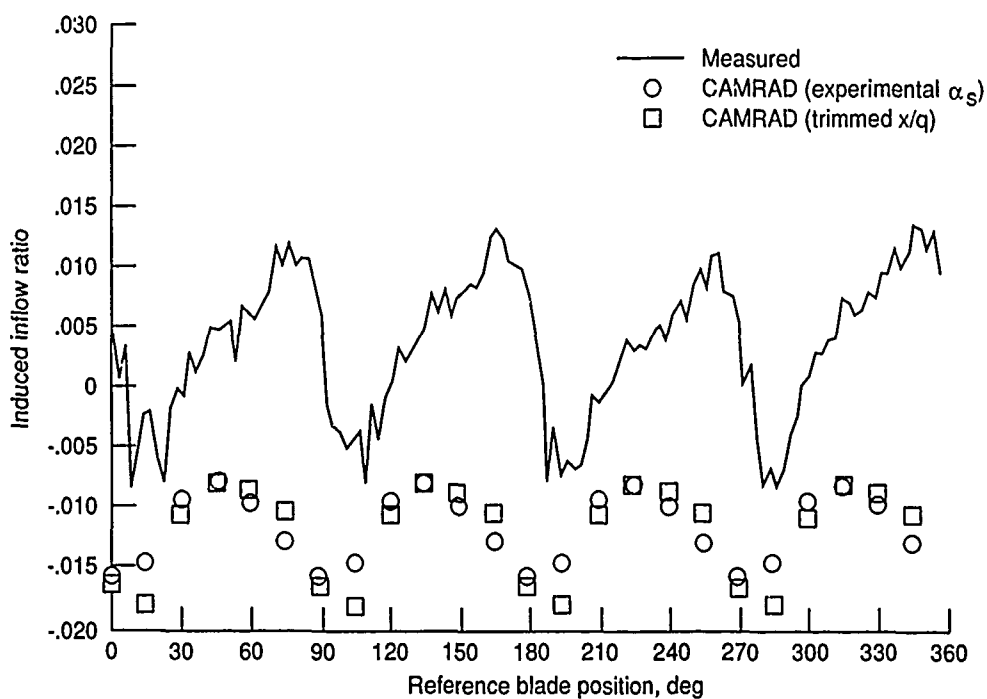


(a) $r/R = 0.40$.

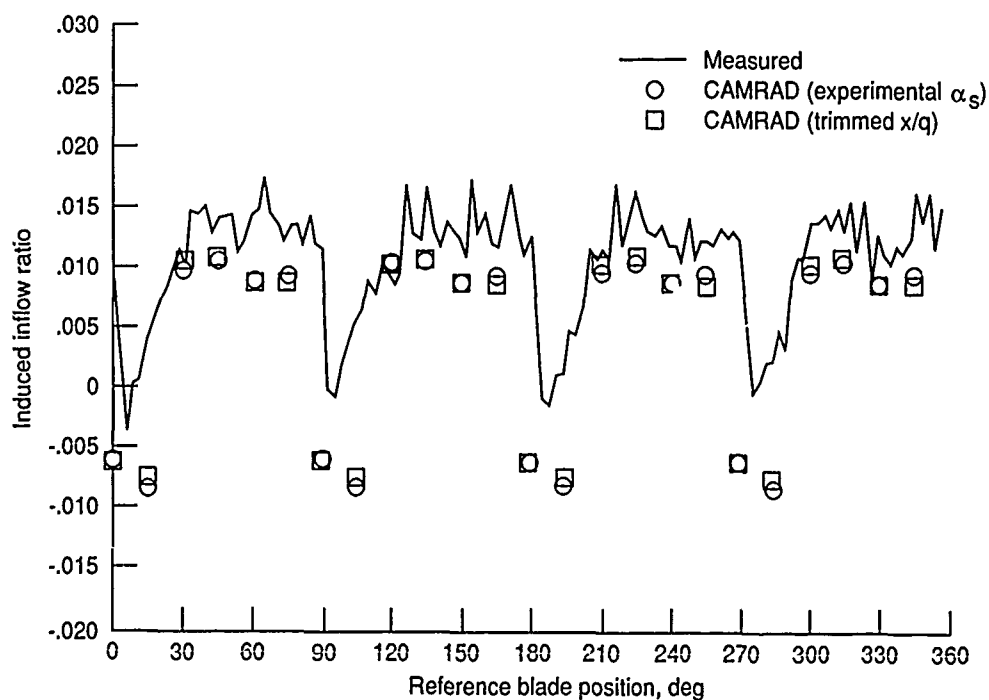


(b) $r/R = 0.90$.

Figure 12. Time history of measured and CAMRAD predicted induced-inflow ratio at $\mu = 0.23$ and 330° azimuth.



(a) $r/R = 0.40$.



(b) $r/R = 0.90$.

Figure 13. Time history of measured and CAMRAD predicted induced-inflow ratio at $\mu = 0.30$ and 180° azimuth.

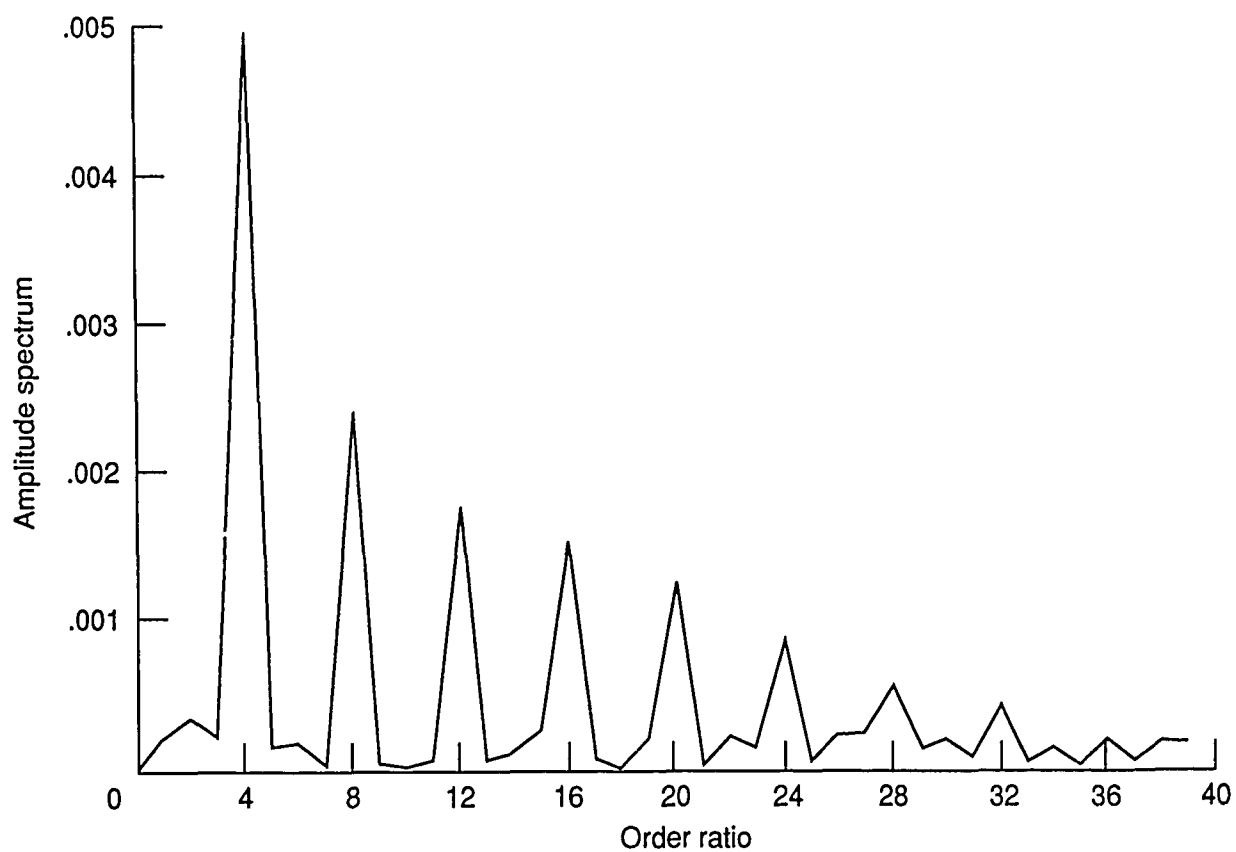
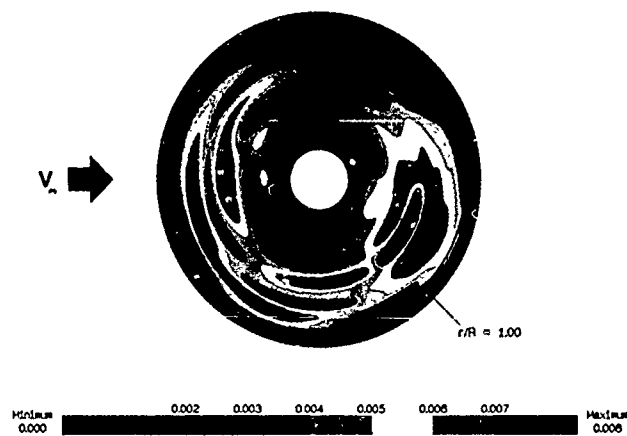
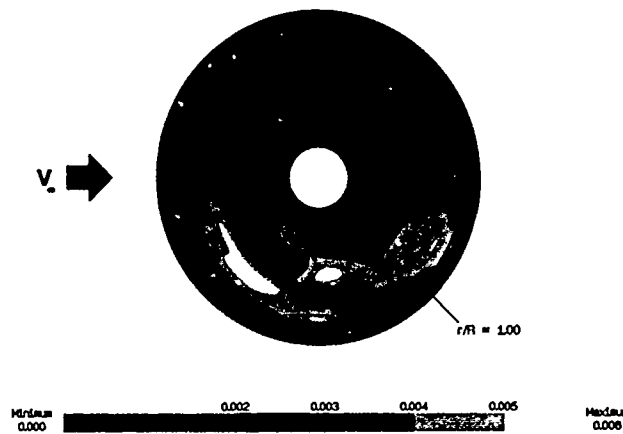


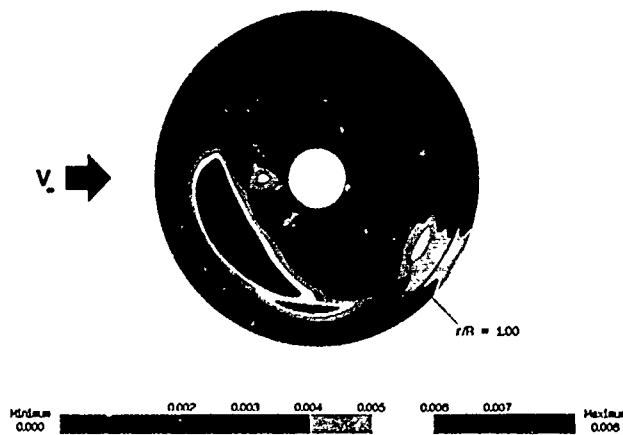
Figure 14. Sample order-ratio analysis of a selected laser velocimeter measurement at $r/R = 0.90$, $\Psi = 150^\circ$, and $\mu = 0.15$.



(a) $\mu = 0.15$; $\alpha = -3.0^\circ$.

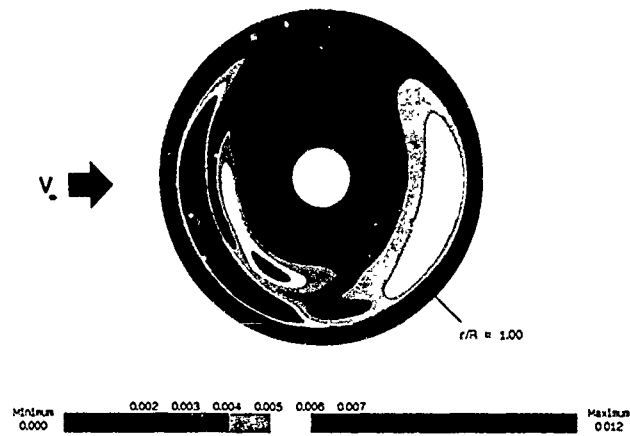


(b) $\mu = 0.23$; $\alpha = -3.0^\circ$.

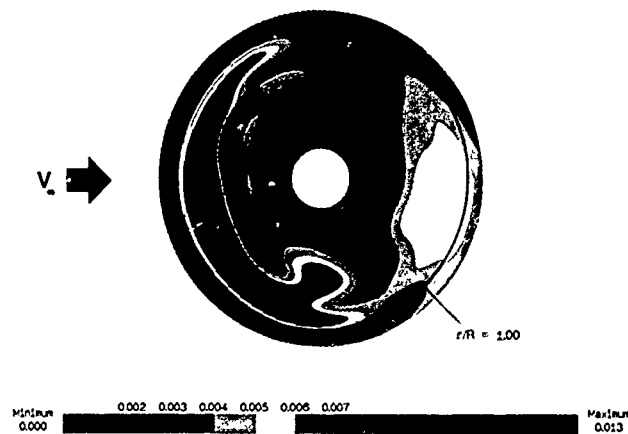


(c) $\mu = 0.30$; $\alpha = -4.0^\circ$.

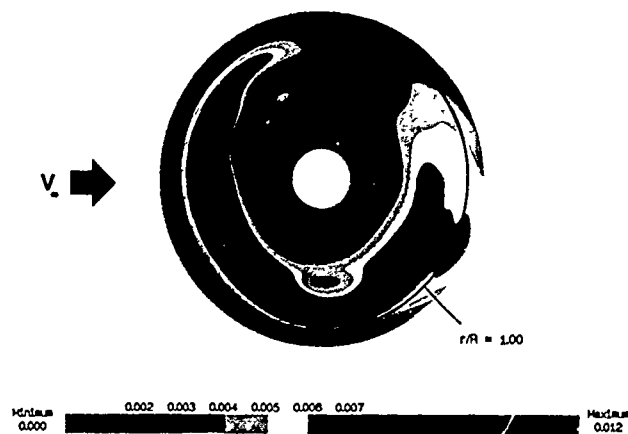
Figure 15. Measured fourth harmonic of the oscillatory induced-inflow-ratio distribution 3 in. above rotor tip-path plane.



(a) $\mu = 0.15$



(b) $\mu = 0.23$



(c) $\mu = 0.30$

Figure 16. Fourth-harmonic oscillatory induced-inflow ratio predicted using CAMRAD with trim option 1.